Ocean Modelling 78 (2014) 1–16

Contents lists available at ScienceDirect

Ocean Modelling

journal homepage: www.elsevier.com/locate/ocemod

Simulating conditional deterministic predictability within ocean frontogenesis

Gregg A. Jacobs [a,*], James G. Richman [a], James D. Doyle [b], Peter L. Spence [c], Brent P. Bartels [c], Charlie N. Barron [a], Robert W. Helber [a], Frank L. Bub [d]

[a] Naval Research Laboratory, 1009 Balch Blvd, Stennis Space Center, MS 39529, United States
[b] Naval Research Laboratory, 7 Grace Hopper Ave. Stop 2, Monterey, CA 93943, United States
[c] QinetiQ North America, 1009 Balch Blvd, Stennis Space Center, MS 39529, United States
[d] Naval Oceanographic Office, 1101 Balch Blvd, Stennis Space Center, MS 39529, United States

ARTICLE INFO

Article history:
Received 12 June 2013
Received in revised form 2 February 2014
Accepted 25 February 2014
Available online 26 March 2014

Keywords:
Altimeter
Frontogenesis
Mesoscale
Assimilation
OSE
Predictability

ABSTRACT

Ocean mesoscale eddies are non-deterministic in that small errors grow in time so that accurate prediction is not possible without continual correction from observations. Ocean frontogenesis can be forced by mesoscale eddies through straining of buoyancy gradients, which produces filaments of surface divergence related to ageostrophic upwelling. The upwelling can result in thinning of the mixed layer. The frontogenesis predictability is tested through a series of Observation System Experiments (OSEs), the results of which indicate that if the strength and location of the mesoscale eddies are accurately predicted, then the associated frontogenesis features can be predicted. The frontogenesis features have a 'conditional deterministic predictability'. The OSEs are started with perturbed initial conditions, and the OSEs assimilate an increasing number of satellite altimeter data streams. One experiment uses all available data to provide the most accurate analysis, which is labeled as the nature run. Relative to the nature run, ocean steric height correlations increases from about 0.87 with one altimeter and asymptotically reaches 0.99 with four altimeters, showing increasing skill in mesoscale prediction. Satellite data provide no information to dynamically correct frontogenesis processes in the numerical models. Even though not corrected by data, as the number of satellite altimeters increases from 1 to 4, the spatial correlation to the nature run of the frontogenesis forcing increases linearly from 0.27 to 0.59, the surface divergence correlation increases linearly from 0.27 to 0.57 and mixed layer depth correlation increases linearly from 0.67 to 0.89. The conclusion is that within the simulations the frontogenesis filaments are deterministically predictable conditioned on accurate prediction of the mesoscale.

Published by Elsevier Ltd.

1. Introduction

Mesoscale fronts associated with strong horizontal density gradients and geostrophically balanced velocity along these gradients are ubiquitous features of the upper ocean. The geostrophic flow strains the buoyancy field resulting in increasing horizontal buoyancy gradients that in turn act as a forcing to ageostrophic motions moving the front back towards a geostrophic balance. The confluence of water masses is a form of frontogenesis, which we will denote as mesoscale forced frontogenesis or deformation-induced frontogenesis (Hoskins and Bretherton, 1972; McWilliams et al., 2009a,b) to distinguish this form from other forms of frontogenesis. Associated with this class of frontogenesis are significant changes in the potential vorticity and vertical velocity. The association of the frontogenesis and potential vorticity changes has been observed *in situ* (Pollard and Regier, 1992; Pallàs-Sanz et al., 2010). The frontogenesis-driven upwelling can also result in filaments of shallow mixed layer depth (MLD) that occur along mesoscale fronts, such as the shallow MLD filament stretching from 125° E to 128° E along 21° 37′ N in Fig. 1. The filaments are 10 to 20 km across and hundreds of kilometers in length. The Western Pacific provides an attractive study area because this region encompasses several mesoscale eddies and fronts associated with the Kuroshio and deep Pacific Ocean, although such features commonly occur in other regions as well (Capet et al., 2008a). Filaments along eddy fronts have been transited by well instrumented ocean gliders in the northwest Mediterranean (Niewiadomska et al., 2008) and by shipboard surveys in the California Current System (Pallàs-Sanz et al., 2010), revealing that biological activity is associated with

* Corresponding author. Tel.: +1 228 688 4720; fax: +1 228 688 4759.
E-mail address: gregg.jacobs@nrlssc.navy.mil (G.A. Jacobs).

http://dx.doi.org/10.1016/j.ocemod.2014.02.004
1463-5003/Published by Elsevier Ltd.

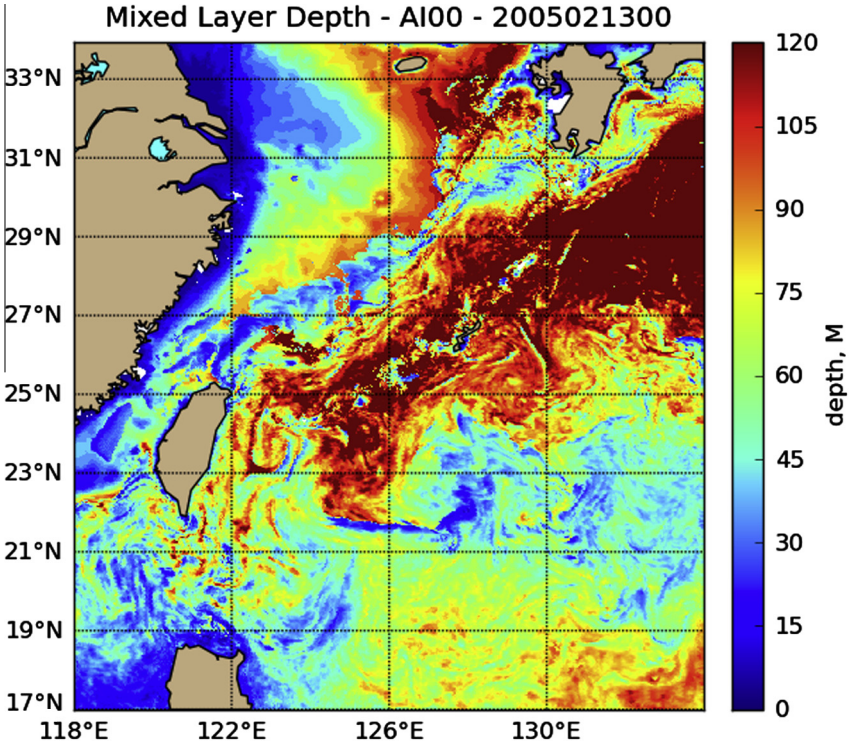

Fig. 1. A snapshot on February 6, 2005, of the model "nature run" mixed layer depth (MLD) with a filament featuring very shallow MLD approximately 20 km across and hundreds of kilometers long near (21° 37′ N, 125–128° E).

the vertical movement of water into the euphotic zone along fronts (Thomas et al., 2008).

The potential frontogenesis impact on the ocean (McWilliams et al., 2009a,b; Zhong and Bracco, 2013) motivates the question whether prediction systems have skill in forecasting filaments and their subsequent impact on the upper ocean and MLD. Prior theory (Hoskins, 1982) and studies (Pinot et al., 1996) have shown that one class of frontogenesis process is dynamically driven by the total derivative of the horizontal gradient of the buoyancy field. The buoyancy field and currents are primarily driven by the mesoscale field. As the mesoscale field strengthens horizontal buoyancy gradients, the forced ageostrophic motion results in vertical movement. Thus, given accurate knowledge of the mesoscale state, frontogenesis should be deterministic if a system is capable of representing the ageostrophic velocity response to the buoyancy straining generated by the mesoscale field. The objective at hand is to quantify the predictability related to frontogenesis and its effects with respect to present observing systems.

The Global Ocean Data Assimilation Experiment (GODAE) (Bell et al., 2009) provided several examples of ocean forecast capability built on numerical models that represent or at least permit the necessary mesoscale physical processes and the observation systems that provide continual corrections of the ocean state on a regularly cycling basis. An overview of the methods applied within the GODAE systems (Cummings et al., 2009) shows that the main objective of data assimilation is to regularly correct the mesoscale structure in the initial condition for the model forecast. Analysis increments in the temperature and salinity fields relate to changes in the velocity field through an assumption of a geostrophic balance, which is not the case for frontogenesis processes (Mensa et al., 2013). The present assimilation systems are not using observations to correct frontogenesis features. Satellite altimeter data are the major contributor to the ocean observing systems and the major source of information to constrain the mesoscale. Altimeter data do not contain significant signals from frontogenesis because the process occurs mainly in the upper ocean with little change in the sea surface height. Because frontogenesis is driven by mesoscale strain, the spatial scales are smaller than the mesoscale, and the spatial structures of the frontogenesis are not resolved by the altimeter ground track sampling patterns.

Taking these considerations together, present cycling forecast systems attempt to accurately correct the mesoscale field through assimilation of routine observations. If the physical processes of frontogenesis are represented properly within a numerical system, then a forecast model will generate frontogenesis in response to the mesoscale straining of the buoyancy field. Thus, the features have very little signal in observations, occur at scales not resolved by the observation system and are not dynamically corrected by the assimilation process, yet can be predicted. Previous studies have demonstrated that increasing the number of satellite altimeter observations leads to greater accuracy in forecasting the mesoscale features such as sea surface height (SSH) (Smedstad et al., 2003; Ananda et al., 2006). If the frontogenesis filaments are non-deterministic then prediction systems will not show skill regardless of the amount of altimeter data. If the filaments are purely deterministic then prediction systems will show skill even in the absence of assimilated data. If the filaments are conditionally deterministic then as data are added to the assimilation, both the mesoscale skill and frontogenesis skill will increase together.

A series of numerical experiments are analyzed to understand the impact of increasing altimetric sea surface height observations on the forecast skill at scales larger and smaller than the mesoscale and time periods shorter than 60 days. The results are consistent with the concept that the frontogenesis is deterministically driven by the mesoscale field within the simulations. As accuracy in the mesoscale field increases with increasing number of satellite altimeter observations, accuracy also increases in frontogenesis forcing, surface divergence and MLD. Thus the evidence supports the conclusion that filaments are conditionally deterministic. It should be cautioned that the context is within the simulation

experiments, and this context constitutes a demonstration in a simulated environment. Within the scope of this paper, demonstration in a real environment is not addressed.

In Section 2, a brief overview of mesoscale driven frontogenesis physics is presented. The model and Observing System Experiment (OSE) setups are discussed in Section 3. The ability of the OSE simulations to reproduce mesoscale and frontogenesis structure is presented in Section 4. A statistical characterization of the forecast skill in mesoscale and frontogenesis is presented in Section 5. Implications for observing systems are discussed in Section 6, and conclusions are in Section 7.

2. Mesoscale-driven frontogenesis

Hoskins and Bretherton (1972) and Hoskins (1982) describe the dynamics of frontogenesis driven by the straining of buoyancy gradients by quasigeostrophic flow. The evolution of buoyancy gradients in a non-divergent geostrophic flow is

$$\left(\frac{D_g}{Dt}b_x, \frac{D_g}{Dt}b_y\right) = (-u_{gx}b_x - v_{gx}b_y, -u_{gy}b_x - v_{gy}b_y) = \overrightarrow{Q_1}, \quad (1)$$

where D_g/Dt is the total derivative using geostrophic velocities u_g and v_g, b_x and b_y are the horizontal gradients of buoyancy, $b = -g\rho'/\rho_o$, and $\overrightarrow{Q_1}$ is the geostrophic frontogenesis or omega vector arising from the straining of the buoyancy gradients by the geostrophic flow. Given this dynamical balance and the simplified equations for the quasigeostrophic momentum and buoyancy evolution, the vertical velocity, w, can be diagnosed from the omega equation,

$$N^2\nabla_h^2 w + f^2\frac{\partial^2 w}{\partial z^2} = 2\nabla\cdot\overrightarrow{Q_1}, \quad (2)$$

where N is the Brunt–Väisälä frequency, and f is the Coriolis parameter. The straining of the buoyancy gradients acts to increase the strength of the front and drives the motion away from geostrophic balance. An ageostrophic secondary circulation is established to move the flow back towards geostrophic balance. Alternately, frontogenesis can be characterized using conservation of Ertel potential vorticity as described in Pollard and Regier (1992). The geostrophic velocity along a front has cyclonic and anticyclonic vorticity on the flanks of the frontal jet. A confluence into the front leads to increasing total vorticity on the cyclonic (low density) flank and decreasing total vorticity on the anticyclonic (high density) flank. Conservation of potential vorticity requires upwelling on the cyclonic (low density) flank and downwelling on the anticyclonic (high density) flank. In a vertical plane, a local maximum of Q_1 is a stream function creating a vertical circulation with associated upwelling and downwelling in addition to a horizontal ageostrophic velocity. The frontogenesis structure and induced ageostrophic vertical velocity have been correlated to changes in mixed layer depth in numerical models with the mesoscale circulation initialized from observations (Paci et al., 2005) with upwelling suppressing the mixed layer depth and downwelling increasing the mixed layer depth.

3. Observation System Experiments (OSE)

Predictability can be tested in several ways. One method is to compare forecast results to independent data. However, significant problems exist for this method when looking at the forecast skill of frontogenesis features. The number of *in situ* profiles from Argo profiling floats, local hydrographic surveys and other ship-of-opportunity data is relatively small. For the domain in Fig. 1, over the period from June 2004 through December 2005, there are about 2500 *in situ* profiles available. Thus, over this domain, there is a low probability that randomly placed observations will actually sample one of these filaments, let alone resolve its spatial structure and evolution. Satellite imagery can potentially provide supporting evidence such as sea surface temperature (SST) along fronts. However, this area is heavily impacted by cloud cover, the SST signature can be small and the imagery does not provide vertical structure information. Hence, an OSE approach is employed where models provide sufficient data for evaluation, although some careful considerations are necessary to avoid false conclusions, which are discussed in Section 3.2.

3.1. Numerical model

The numerical model for the OSEs is the Navy Coastal Ocean Model (NCOM) (Barron et al., 2006), which is the same model as the global model used as boundary conditions and is run operationally. A doubly-nested domain is constructed for the OSEs (Fig. 2). The outer domain with 10 km resolution extends from 11.5° S to 50° N and 98.5° to 165° E. The outer domain is forced by boundary conditions from the global model (Barron et al., 2007). The inner domain with 3.16 km resolution extends from 17° to 34° N and 118° to 134° E and is forced by boundary conditions from the outer domain. For both domains, the same vertical setup is used with 34 sigma levels and 15 Z levels beneath (49 total levels). Sigma levels cover the surface to 595 m depth, and the Z levels cover the lower water column. The thinnest layer at the surface has a thickness of 0.52 m, and deeper layers telescope to the thickest sigma layer of 85 m at a depth of 510 m. The high resolution near the surface is intended to properly represent frontogenesis physics. All OSEs are forced by the same atmospheric conditions from the Navy Operational Global Atmospheric Prediction System (NOGAPS, Rosmond et al., 2002; Goerss, 2009) across the outer domain and the Coupled Ocean Atmosphere Mesoscale Prediction System (COAMPS; Hodur, 1997) across the inner domain. The surface wind stress is determined from the atmospheric model wind velocity. Surface heat fluxes are computed using bulk flux formulations that use the 10-m air temperature and humidity along with the ocean model SST. Tidal potential forcing is applied to the inner domain of all OSEs, and tidal boundary conditions for water level and barotropic velocity are provided by the Oregon State University global Ocean Tide Inverse Solution (OTIS) (Egbert and Erofeeva, 2002). Thus, locally generated internal tides are present in the model.

Data assimilation is performed with daily cycling. All data 12 h before and 12 h after 00Z for the present day are used in the analysis. The analysis is accomplished through a multi-variate optimal interpolation (MVOI) (Cummings, 2005). Observation increments are computed by differencing observation values and a background field provided by a prior model forecast at the same time as the observations. The horizontal covariance length scales are based on latitudinally varying Rossby radius of deformation and vertical scales are based on vertical gradients. The Rossby radius varies from 80 km at the southern extent of the domain to 31 km at the northern extent. A factor of 0.82 is used to scale the Rossby radius to provide the decorrelation length scales in the MVOI resulting in an average decorrelation scale of 45 km. Satellite SSH and SST observations are used to construct synthetic profiles through subsurface covariances (Fox et al., 2002) which are used in the MVOI.

The analysis increment is inserted into a 24 h hindcast by rerunning the model over the prior 24 h and adding the analysis divided by the number of time steps to the state variables throughout the 24 h hindcast. This represents a correction to the slowly evolving state field rather than resetting the initial condition at 00Z. This also affects features mainly at scales larger than the horizontal decorrelation length. Features smaller than the decorrelation length are not significantly altered by the assimilation just as the short time period variations are not altered. Direct insertion

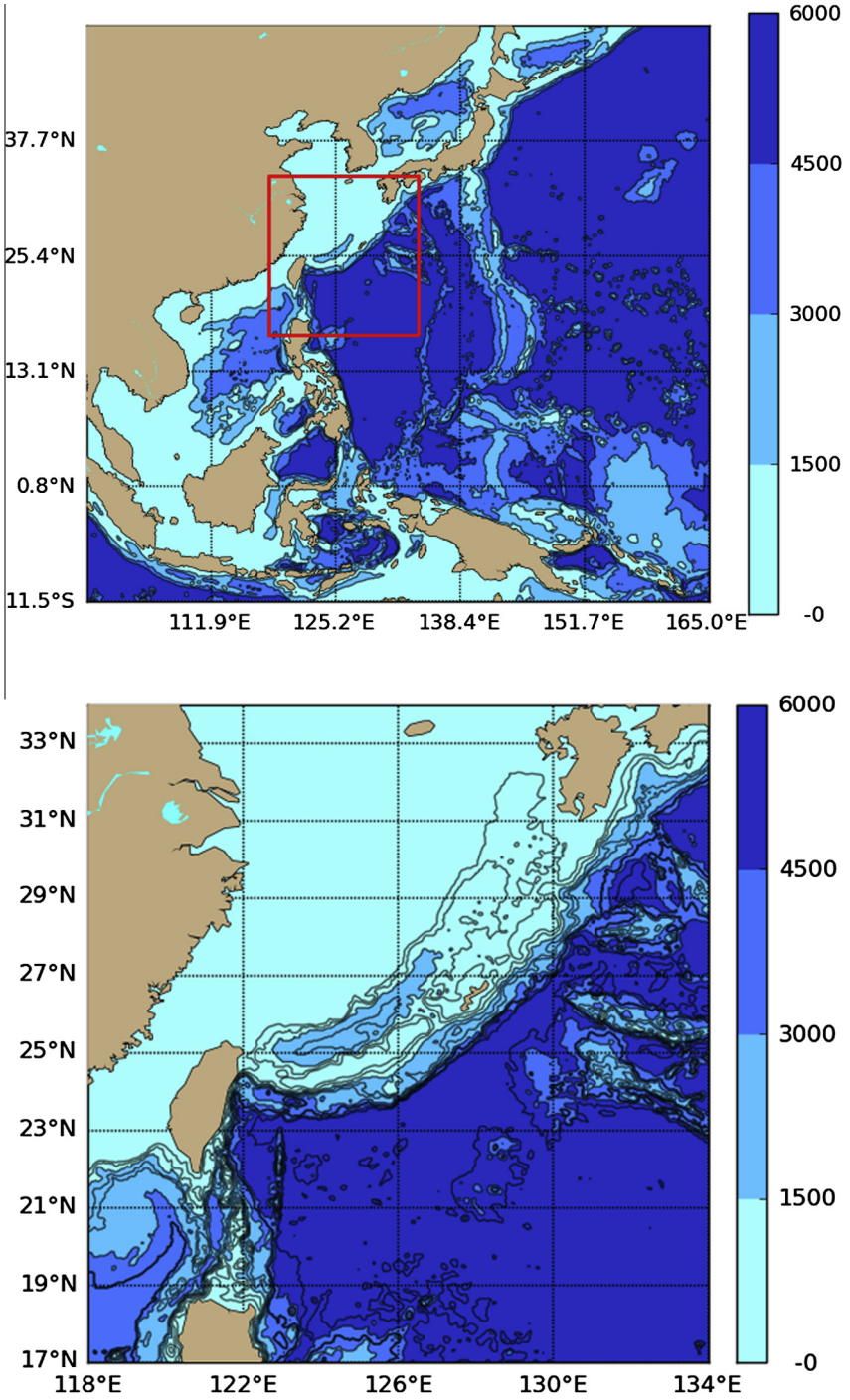

Fig. 2. A doubly-nested domain is constructed for the OSEs. The outer domain with 10 km resolution (top) is used as a buffer between the global model solution with about 12 km resolution, which provides boundary conditions, and the inner domain with 3.16 km resolution (bottom). The doubly nested domain allows the perturbations in data availability to alter the boundary conditions from the global model before they are passed to the inner domain to properly reflect the observing system capability.

of the corrections and resetting the initial conditions can generate spurious internal and inertial waves that, in ocean models, require several days to damp out. The 24 h forecast then provides the background for the next assimilation cycle.

Because the global system assimilates all available data from the observing systems, the lateral boundary conditions of the outer domain for all experiments are influenced by all available data. The large outer domain is used to isolate the inner nest from the influence of the global simulation. The data assimilated in the outer domain of each OSE is the same limited data as used in the inner domain. The distance between the boundary of the outer domain and inner domain is several Rossby radii so that most of the mesoscale features in the OSE domain are generated in the domain rather than propagating from the boundary. The 31° longitudinal distance from the eastern outer to eastern inner boundary would require longer than 1 year to transverse the domain at a propagation speed of 0.1 m/s.

3.2. Observing system experiment setup

In an OSE approach, one experiment is referred to as the nature run, which is the experiment that is as close to the natural world as

can be achieved. In addition, the nature run differs from the other OSE experiments so that processes that are nondeterministic will evolve differently from the other OSE runs, which is achieved by providing an initial condition for the OSE experiments that is different from the nature run initial condition. The nature run performance is very important, and this is evaluated below. The model, data assimilation method and atmospheric forcing are held constant across the OSEs so errors in these components relative to the nature run are eliminated. Each experiment is run independently from all others with the only difference being the observation data streams included in the experiment. The impact of each data stream is then evaluated relative to the nature run.

There is risk of reaching a false positive result through the OSE approach. If the forecast system were to incorrectly produce frontogenesis in the same places without regard to the background flow, it could incorrectly be concluded that predictability exists when in fact it does not. Therefore, OSE experiments must demonstrate that if the mesoscale field is not accurately forecasted then the filaments likewise are not forecasted. There is risk of reaching a false negative if the system is not sensitive to the control variable (quantity of altimeter streams that controls mesoscale positioning accuracy). It is required that the filament accuracy must increase as additional data sets are added. These two requirements must be demonstrated by the OSE results.

The control variable is the quantity of mesoscale observations, an approach motivated by previous studies showing that the quantity of satellite altimeter data strongly influences the reconstruction accuracy of the mesoscale field. The OSE time period spans 1 June 2004 through 31 December 2005. During this period, four altimeter satellites were operating: ENVISAT, Jason-1, TOPEX/Poseidon in the interleaved orbit (TPXI), and the Geosat Follow-On (GFO). While each satellite suffered periodic outages on the order of a day for a variety of reasons, the data return rate was relatively consistent throughout this time with the exception of the TOPEX/Poseidon interleaved data which ends in October 2005, prior to the last 2 months of the experiments.

The set of experiments using different permutations of available data sets is presented in Table 1. In addition to the satellite altimeters, data from the Advanced Very-High Resolution Radiometer (AVHRR) satellite SST processed by the Naval Oceanographic Office (May et al., 1998) and *in situ* temperature and salinity profiles are used in the assimilation. The OSEs differ from the nature run (labeled as OSE00 in Table 1) by a combination of data sets assimilated and the initial condition for the experiments. The nature run uses the state from the global ocean model valid on 01 June 2005 as an initial condition, while all other OSEs use a different initial condition, the global model state from the previous year, 01 June 2004. This difference in initial condition between the nature run and all other OSEs ensures that any process that is inherently non-deterministic and not constrained by the observation data will not be correlated between the nature run and the OSEs.

3.3. Observing system experiment evaluation

One qualitative example of ability of the nature run to synoptically place the mesoscale features is provided in Fig. 3. Snapshots of NOAA AVHRR Local Area Coverage (LAC) satellite SST (Fig. 3a) and model SST (Fig. 3b) for March 9, 2005, indicate a strong temperature front in roughly the same location and some of the small features along the front. However, much of the domain is covered by clouds preventing comparison. Sea surface height and profile data for any given day are sparse. An objectively interpolated map of the altimeter SSH (Jacobs et al., 2001) with altimeter tracks for 7 days before and after March 9, 2005 and the quality controlled altimeter data locations for the time period is shown in Fig. 3c. The altimeter map contains frontal positions in agreement with those in the satellite SST, but does not resolve the small scale features associated with the front observed in the model SST and steric height (Fig. 3d). The model MLD has greater small scale variability than the observed SSH. Generally shallow mixed layers are found in the frontal zone with filaments of small MLD. The shallow MLD features have corresponding features in the model SST, though the amplitude of SST impact is small. The satellite SST color bar range in Fig. 3 is relatively large because of the temperature change across the front. The influence of the data assimilation analysis should also be considered. The analysis decorrelation scale is about 50 km at the latitude of Fig. 3. The analysis is inserted into the 24 h hindcast with equal increments at each model time step. The result should be that features smaller than the decorrelation scale should dynamically remain unchanged. Only the large scale flows should be altered. Thus the assimilation should not significantly alter the filament features.

The nature run MLD is compared to values estimated from the 2500 *in situ* profiles taken in the domain between 1 June 2004 and 31 December 2005, with the locations of the profiles displayed in Fig. 4a. MLD is taken to be the depth where temperature deviates by 0.3° C from the near surface temperature. Near surface temperature is used rather than the surface temperature to avoid extremely shallow MLD (<5 m) due to diurnal warming that affects only the upper few meters. Other definitions for MLD such as isopycnal or isohaline mixed layer depths exhibit very similar results in this area. Two comparisons to the *in situ* observed MLD are

Table 1
The difference between OSE experiments is the input data (altimeter, SST, *in situ*) used in the assimilation. The time-average of spatial anomaly correlation increases for a range of variables as data streams are added.

Exp ID	Altimeter data sets	SST	*In situ* data	Correlation between nature run and OSE for parameters			
				Mixed layer depth	Steric height	Divergence	Q_1
OSE00/nature run	Jason GFO ENVISAT TPXI	On	On				
OSE01	None	None	None	0.21	0.15	0.03	0.03
OSE02	None	On	On	0.27	0.42	0.05	0.08
OSE03	Jason GFO ENVISAT TPXI	On	On	0.89	0.99	0.57	0.59
OSE04	Jason	On	On	0.66	0.84	0.25	0.27
OSE05	GFO	On	On	0.68	0.89	0.29	0.28
OSE06	Jason GFO	On	On	0.76	0.94	0.37	0.36
OSE07	ENVISAT	On	On	0.66	0.85	0.26	0.26
OSE08	Jason ENVISAT	On	On	0.74	0.93	0.35	0.35
OSE09	GFO ENVISAT	On	On	0.74	0.94	0.37	0.37
OSE10	GFO Jason ENVISAT	On	On	0.81	0.97	0.45	0.45
OSE11	GFO TPXI	On	On	0.74	0.94	0.34	0.35
OSE12	GFO Jason TPXI	On	On	0.81	0.98	0.44	0.45
OSE13	Jason TPXI	On	On	0.73	0.93	0.33	0.34
OSE14	GFO ENVISAT TPXI	On	On	0.80	0.96	0.42	0.41

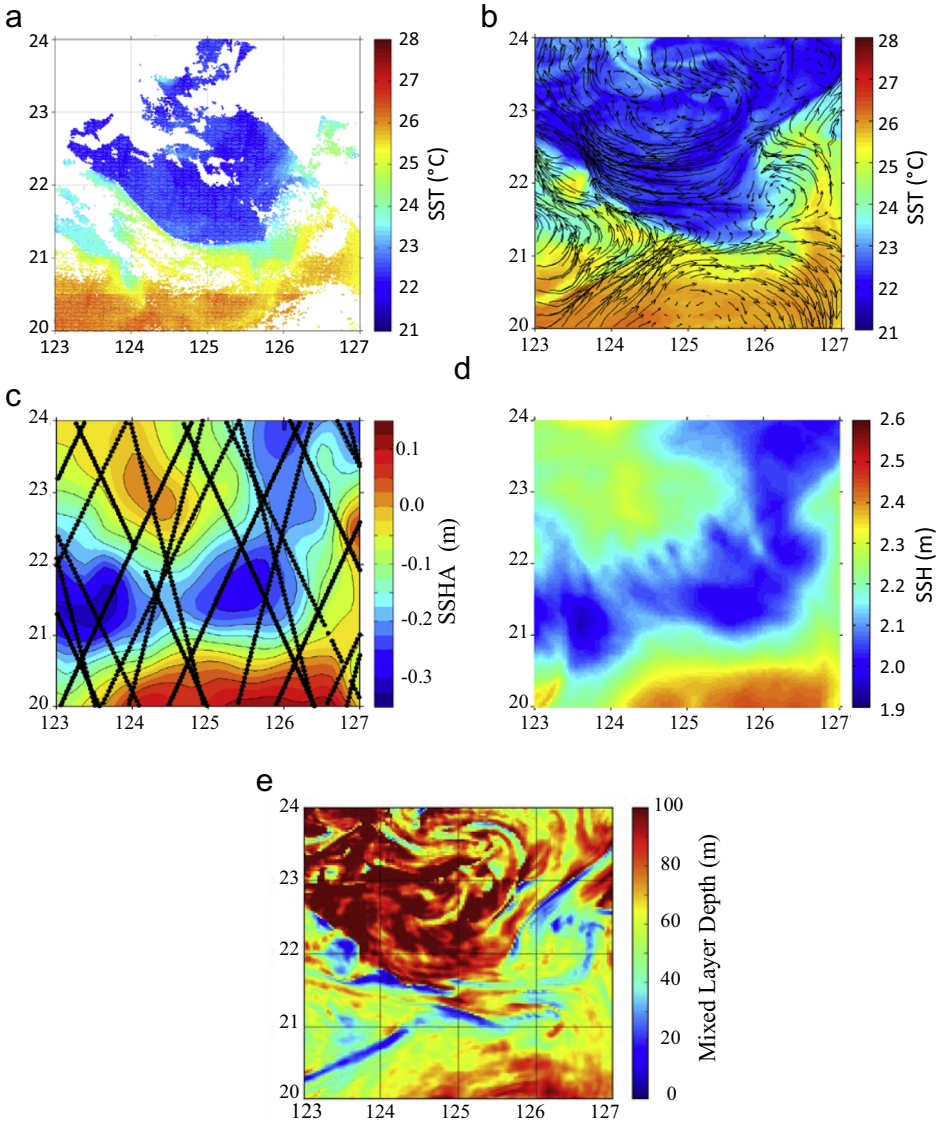

Fig. 3. Snapshots on March 9, 2005 of SST with surface currents (b), steric SSH referenced to 1000 m (d) and MLD (e) from the model "nature run" on March 9, 2005, and satellite AVHRR SST (a) and satellite altimeter SSH anomaly with tracks (c) for the same day. The satellite and model SST and SSH all indicate a strong front along a mesoscale feature in the same location though none exhibit the presence of filaments that exist in the MLD.

provided, one prior to the assimilation of the profile data and the other after the assimilation. Because the profiles are very sparse in space and time, the observations are in general independent. A few apparent cases may be contrary to this. For example, there are ship-of-opportunity tracks transecting through the Luzon Strait. As the ships cross the area, observations assimilated on a prior day to correct the model may be correlated with nearby unassimilated observations. However, this does not seem to be the general case. The scatterplots of the model and observed MLD indicate moderate skill in predicting the MLD. For the MLD prior to assimilation of data, the RMS error is about 27.6 m with a correlation coefficient of 0.75, while the RMS error after assimilation is smaller at about 25.8 m with a slightly higher correlation coefficient of 0.78. Data assimilation, in general, does not make a very large correction day-to-day.

4. Frontogenesis in the OSEs

Numerous mechanisms have been proposed to generate vertical motion at fronts, which can be grouped into three general classes: flow interaction, intrinsic instabilities and forcing interaction. Besides the large-scale strain-driven frontogenesis of Hoskins and Bretherton (1972), vertical mixing associated with along-frontal velocity shear can generate a cross-frontal ageostrophic velocity below the Ekman layer and frontogenesis on the dense side of the front (Garrett and Loder, 1981). Baroclinic instability can occur at any front when available potential energy is converted into kinetic energy. Scaling analysis for baroclinic instability indicates that the Burger number, $Bu = (NH/(fL)) = RoRi^{1/2} \sim O(1)$, where the Rossby number, $Ro = (U/(fL))$, and the Richardson number, $Ri = (NH/U)^2$, are obtained from a vertical length scale, H, a horizontal length scale, L, vertical stratification frequency, N, and horizontal velocity scale, U. For quasigeostrophic flow with small Ro, Ri is large and the time and length scales of the instabilities are consistent with the mesoscale. However, for Ro of order 1, then Ri is order 1 and the time scale of the instability is short, less than a day, and the length scale is short, typically a few km, consistent with frontogenesis (McWilliams et al., 2009a,b). Boccaletti et al. (2007) find that the mixed layer instabilities are frontolytic with cyclonic vorticity, tending to restratify the mixed layer and move the flow

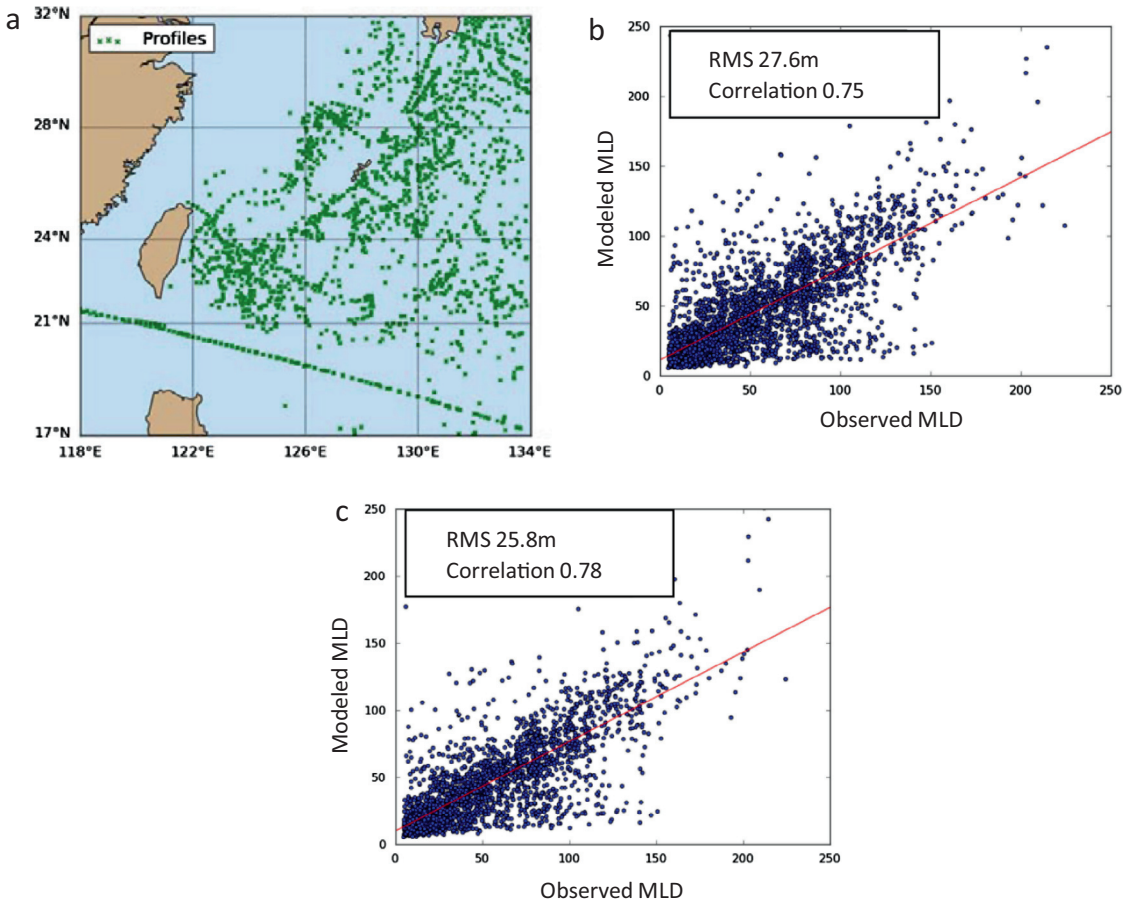

Fig. 4. Evaluation of the nature run MLD performance is made by comparison to *in situ* profile data during the experiment time period. The data locations are relatively randomly distributed with the exception of some ship of opportunity tracks (a). The model is sampled at the same times and locations. The scatterplots of the model 24 h forecast prior to the data being assimilated (b) and the model hindcast after the data have been assimilated (c) with the observed MLD indicate moderate skill in predicting the MLD. For the MLD prior to assimilation of data, the RMS error is about 27.6 m with a correlation coefficient of 0.75, while the RMS error after assimilation is smaller at about 25.8 m with a slightly higher correlation coefficient of 0.78. Assimilation, in general, does not make a very large correction day-to-day.

away from geostrophic balance. When the wind blows down the front, the cross-front advection of density by the Ekman flow carries dense fluid over light fluid leading to destabilizing wind-driven buoyancy flux resulting in convection and enhanced vertical mixing. If Ro is large, then the Ekman transport is modified by the relative vorticity of the flow along the front. The negative relative vorticity on the dense side of the front increases the effect of rotation and decreases the Ekman transport, while the positive relative vorticity on the light side of the front leads to the opposite effect. The resultant ageostrophic secondary circulation is frontogetic with subduction on the dense side of the front and upwelling with shallow mixed layers on the light side of the front. Increasing the strength of the down-front wind increases the frontogenesis. Mahadevan and Tandon (2006) showed that all mechanisms can be active in a high resolution model at the same time.

The theory of quasigeostrophic frontogenesis by Hoskins and Bretherton (1972) predicts an ageostrophic secondary circulation driven by straining of the mesoscale flow in the presence of a density front. In the model simulations, long, narrow filaments of shallow MLD are often observed, such as the filament in Fig. 1 near 21° 37′ N extending from 125° to 128° E. To examine the dynamical balances in detail, a meridional transect along 125° E is examined. The transect shows a strong buoyancy front near 21.8° N with shallow MLD on the light side of the front to the south and deep MLD on the dense side to the north (Fig. 5a). The MLD line plotted in each panel of Fig. 5 is the same. To the north the MLD average is 110 m, and to the south the MLD average is 60 m. The reason for the large scale MLD variation is mesoscale structure changing background stratification. The steric height in Fig. 6 (upper left panel) shows the anticyclone covering the northern half of this transect. This deepens the thermocline and reduces stratification as can be seen in Fig. 5a. The reduced stratification allows turbulent energy to mix deeper resulting in deeper mixed layer to the north of the front.

The shallowest MLD of 30 m extends over a very narrow distance from 21.6° to 21.7° N, and this is the location where frontogenesis is active. Examination of the meridional (cross-frontal) velocity shows mesoscale straining of the velocity across the front (Fig. 5b). Flow is coming into the front from both the south and north. The omega vector, Q_1, from Eq. (1) is calculated (Fig. 5c). High frequency variability in the omega vector, Q_1, is reduced by filtering with a 48 h moving average. The similarly filtered vertical velocity is computed from the model fields (Fig 5d). To the south side of the large amplitude Q_1 at 21.7° N, a strong upwelling exists beneath the upwelled MLD at 21.6° N. On the north side of the large Q_1, a downwelling exists, though it does not extend far below the mixed layer. The upwelling and downwelling are consistent with the frontogenesis forcing at this location and the frontogenesis vertical velocity in McWilliams et al. (2009a,b) (Fig. 3 in the paper). The ageostrophic circulation, associated with the quasigeostrophic frontogenesis, predicts upwelling on the low density side of fronts, the shallow MLD occurs on the warm side of the front.

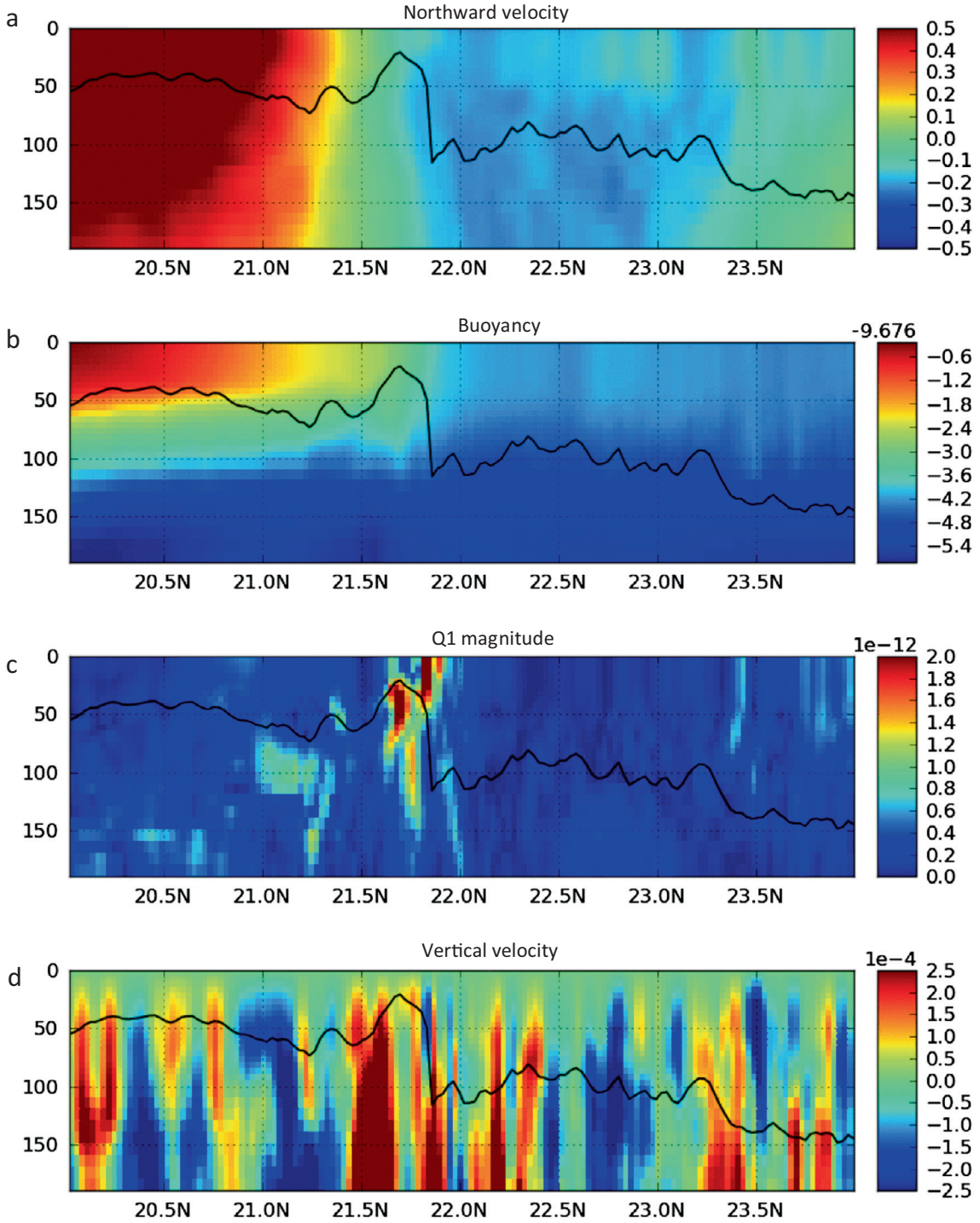

Fig. 5. A meridional cross section along 125° E of the nature run on February 13, 2005 provides an indication of how the omega vector Q_1 is related to the shallow MLD. High frequency and tidal variability is removed using a 48 h boxcar filter. The buoyancy (a) shows a front between 21.5° and 22.0° N. The meridional velocity section (b) shows convergence at this front which increases the horizontal buoyancy gradients. The frontogenesis forcing or omega vector Q_1 (c) increases at the front and is associated with the shallow mixed layer depth. The black line in all plots is the diagnosed mixed layer depth.

These results are consistent with previous modeling (Spall, 1995; Paci et al., 2005; Capet et al., 2008b) and observational frontal analyses of Pallàs-Sanz et al. (2010).

The shallow MLD filaments are common features of the high resolution ocean model. As seen in Fig. 5, the shallow MLD filament 21.7° N is associated with the low density side of fronts and large value of frontogenesis forcing Q_1. In Fig. 6, maps of SSH, Q_1, surface divergence and MLD from a small section of the inner domain are displayed for four of the OSEs on February 13, 2005, the same time as Figs. 1 and 5. The surface divergence is directly related to the vertical velocity just below the surface of the model since the numerical solution process computes vertical velocity as the integral of horizontal divergence from the ocean bottom to each depth, and the time rate of change of model SSH is the horizontal divergence integrated to the surface. In Fig. 6, the nature run results (left column) show good correspondence between small scale spatial

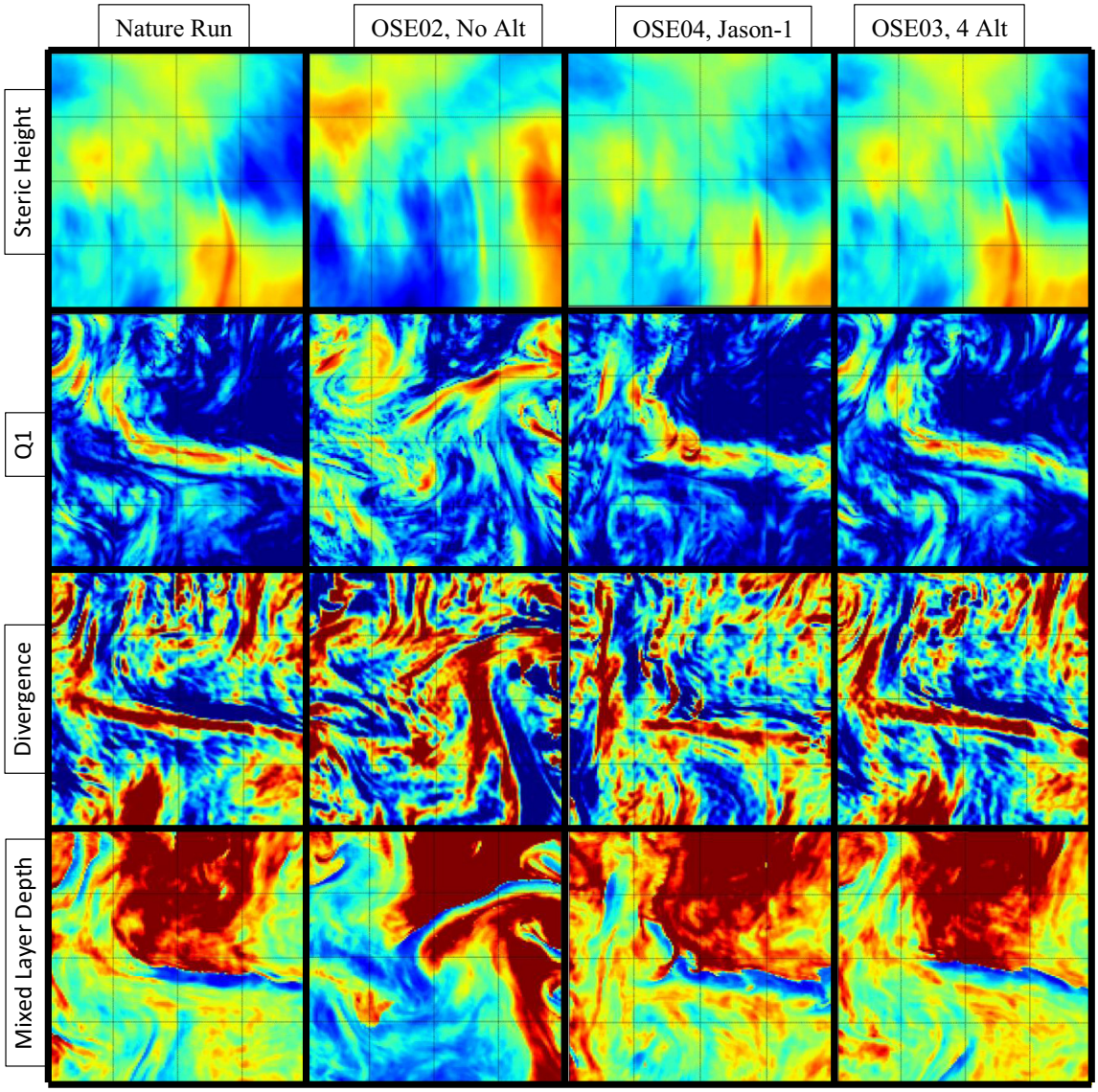

Fig. 6. February 13, 2005 maps of steric height relative to 1000 m (top row, color bar range 1.92–2.58 m), frontogenesis Q_1 (second row, log color bar range −13 to −12), surface divergence (third row, color bar range -12×10^{-6} to 12×10^{-6} m/s/m) and MLD (bottom row, color bar range 0–100 m) for small region (20–24° N and 123–127° E) of the inner domain for four OSEs. The meridional section in Fig. 5 passes through this domain for the nature run (leftmost column). Filaments of shallow MLD, large frontogenesis and large surface divergence (upwelling) are found in the OSEs, but at different locations and strengths. The magnitude of Q_1 is averaged over the upper 100 m to reduce the noise in the estimate, while all other maps are snapshots.

structures in vertical velocity and MLD through comparison of the divergence and MLD.

Many factors influence the spatial structure of the MLD, the strength of the surface wind stress and buoyancy flux, the vertical stratification below the mixed layer and the vertical velocity at the base of the mixed layer. The surface fluxes and vertical stratification set the mixing and entrainment rates for most mixed layer models, while the vertical velocity and entrainment rate set the rate of mixed layer deepening. Mesoscale eddies deform the thermocline and can change the strength of the vertical stratification below the mixed layer. The histogram between steric height (an indirect measure of the thermocline depth and thus stratification in the upper water column) and MLD, shown in Fig. 7, indicates that deeper mixed layers are associated with higher steric heights where anticyclonic eddies weaken the stratification and increase vertical mixing, while shallower mixed layers are associated with lower steric heights as cyclonic eddies increase the stratification and weaken vertical mixing. Given this strong relation, the impact of vertical velocity from frontogenesis is a secondary influence. Very deep MLD can create a situation where the frontogenesis may not be sufficiently strong to alter the deep MLD. This situation occurs across the Kuroshio and its southern recirculation gyres in Fig. 1 north of 29° N. Likewise a very shallow MLD that appears in summer is not strongly impacted. MLD changes due to mesoscale eddies and seasonal effects are contributors in addition to possible effects of frontogenesis. Thus, MLD is only an indicator of frontogenesis predictability, while Q_1 and divergence are more dynamically related.

The MLD filaments occur most often around the fronts associated with eddies where weak forcing has the opportunity to influence the MLD as it transitions from deep within an anticyclone to shallow outside. Frontogenesis is in competition with other mechanisms in controlling MLD. The frontogenesis process is resulting in forcing diagnosed through the omega equation, and upwelling and downwelling are associated with this forcing. In a simple bulk model of the MLD, MLD moves down as water entrains and moves

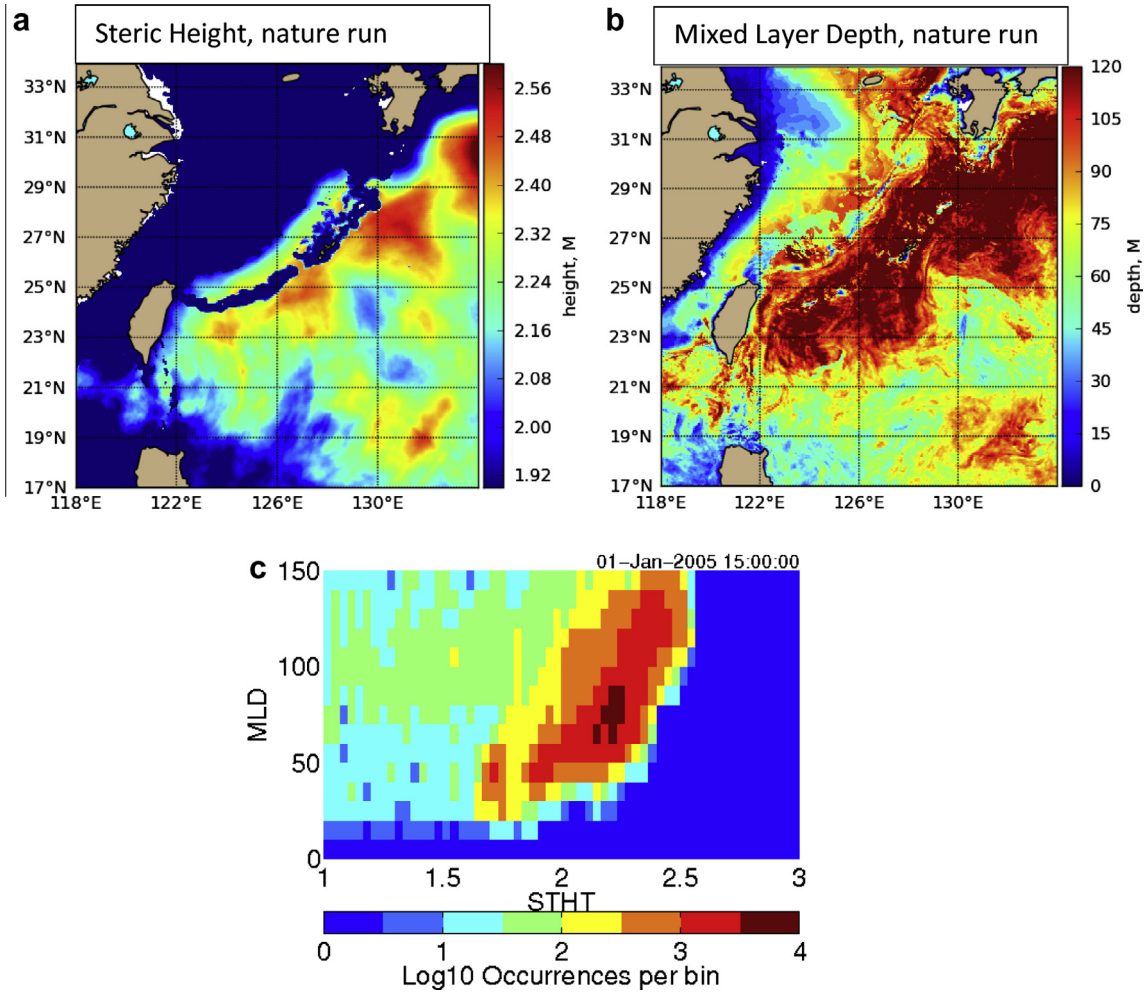

Fig. 7. For the nature run on January 1, 2005 00Z, a snapshot of steric height (a) compared to model MLD (b) shows the relation between mesoscale structure and MLD during winter. The histogram (c) shows that deeper MLD is associated with the higher steric heights as anticyclonic eddies create a weaker background stratification increasing vertical mixing with the opposite true for cyclonic eddies with enhanced stratification and weaker mixing. Frontogenesis competes with the mesoscale stratification to control the MLD.

upward with the upwelling velocity. The upwelling is a factor in determining MLD. The statistical connection through these effects is significant though at times weak as a wide range of processes impact MLD. Therefore, predictability must be measured for each of the contributing components including mesoscale circulation through steric height, the frontogenesis forcing through Q_1, vertical flow induced by frontogenesis through surface divergence (vertical velocity at the base of the model surface layer) and possible secondary impact through MLD.

5. Predictability

In each OSE, fronts exist with associated frontogenesis forcing, divergence and possible resulting impact on MLD filaments. The position and strength of the fronts and associated filaments vary between the OSEs. For each OSE, the only difference is the amount of data assimilated, which is used to locate the position of the mesoscale features. As the amount of altimeter data assimilated increases, the correspondence between the maps increases even in fields not directly observed by the satellites.

The 3 km resolution numerical ocean model meets the first two considerations presented in the introduction. The numerical model is capable of representing the dynamical processes leading to the frontogenesis and has sufficient resolution. The dynamics of the model agree with prior theory of frontogenetic forcing. The associated vertical velocity and surface divergence characteristics of the filaments agree with prior *in situ* and model examinations of frontogenesis variability (Paci et al., 2005). Hoskins and Bretherton (1972) theory of frontogenesis indicates that given the velocity and density field, the forcing driving the frontogenesis is predictable.

The OSEs vary the amount of altimeter observations used in the data assimilation, which influences the synoptic reconstruction of the frontogenesis filaments. Prior studies show that increasing altimeter data increases the fidelity of SSH predictions in assimilation systems (Smedstad et al., 2003; Ananda et al., 2006). An initial qualitative comparison of steric height (Fig. 8) indicates that the OSEs perform as expected. Withholding all altimeter data results in a realistic mesoscale field in terms of the spatial scales and amplitudes of features; however, the mesoscale field is not synoptically correct when compared to the nature run. With a single altimeter, the main features within the steric height align with the nature run, though examination of the finer details show that the edges of features are misplaced and the general shape of the features diverge from the nature run. Comparison of the nature run steric height to that of the OSE03 experiment, which assimilates all four altimeters, indicates that the detailed characteristics of the nature run are reproduced in OSE03 with high fidelity.

An initial qualitative examination of frontogenesis predictive skill (Fig. 6) in a small area indicates the same progression with increasing altimeter data. Comparing the nature run (Fig. 6, left column) to the run with no altimeter data assimilated, OSE02 (Fig. 6, second column), shows that the steric height features are not correctly placed, and the frontogenesis forcing Q_1, surface divergence, MLD and the mesoscale fronts are not correlated with the nature run. With only one altimeter (Jason-1, OSE04 in Fig. 6, third column), the rough position of the main zonal filament is quite similar. However, the OSE04, only Jason-1 assimilated, results indicate discrepancies compared to the nature run in all variables. For OSE03 with all four altimeters assimilated (Fig. 6, right column), a frontogenesis filament occurs in a very similar position to the nature run between 21° and 22° N, and much of the Q_1, surface divergence and MLD structure are correlated well with the nature run. Thus, the OSEs meet two required criteria discussed in Sections 3.2:1) with no altimeter data assimilated the OSE skill fails across all variables, and 2) all evaluation metrics improve as the amount of altimeter data assimilated increases. This provides some confidence that a false positive or false negative conclusion is avoided.

The nature run has a significant annual cycle with MLD deepest in winter (Dec–Feb) and shallowest in summer (Jun–Aug). Thus, the forecast skill of the steric height, Q_1, surface divergence and MLD may vary significantly in time as well as in spatial scale. To quantify this skill on scales larger than the filament scale, scales on the order of the filaments and subseasonal timescales, a small area is chosen for examination, (20–24° N and 123–127° E), which is active in the formation of filaments as well as propagating mesoscale eddies. Comparisons of MLD averaged over this area provide an estimate of the large-scale structure, and comparison of the OSEs to the nature run after removing the large scale MLD reveal progressively greater agreement with added altimeter data (Fig. 9).

With data from one altimeter satellite assimilated, the MLD averaged over the subdomain is comparable between the nature run and OSEs (Fig. 9a), and the annual cycle is reproduced well. Peak discrepancies are about 10 m compared to peak discrepancies of 25 m when no altimeter data are assimilated (not shown). With two altimeters assimilated, peak differences between OSE06 and the nature run are reduced to about 5 m (Fig. 9b). In the experiment assimilating all four altimeters, MLD averaged over the subdomain is well reproduced with peak differences from the nature run being less than 1 m (Fig. 9c).

Spatial correlation between the OSEs and the nature run after removing the area averaged MLD at each time provides the skill on scales smaller than the 4° area. The 3-hourly correlations are

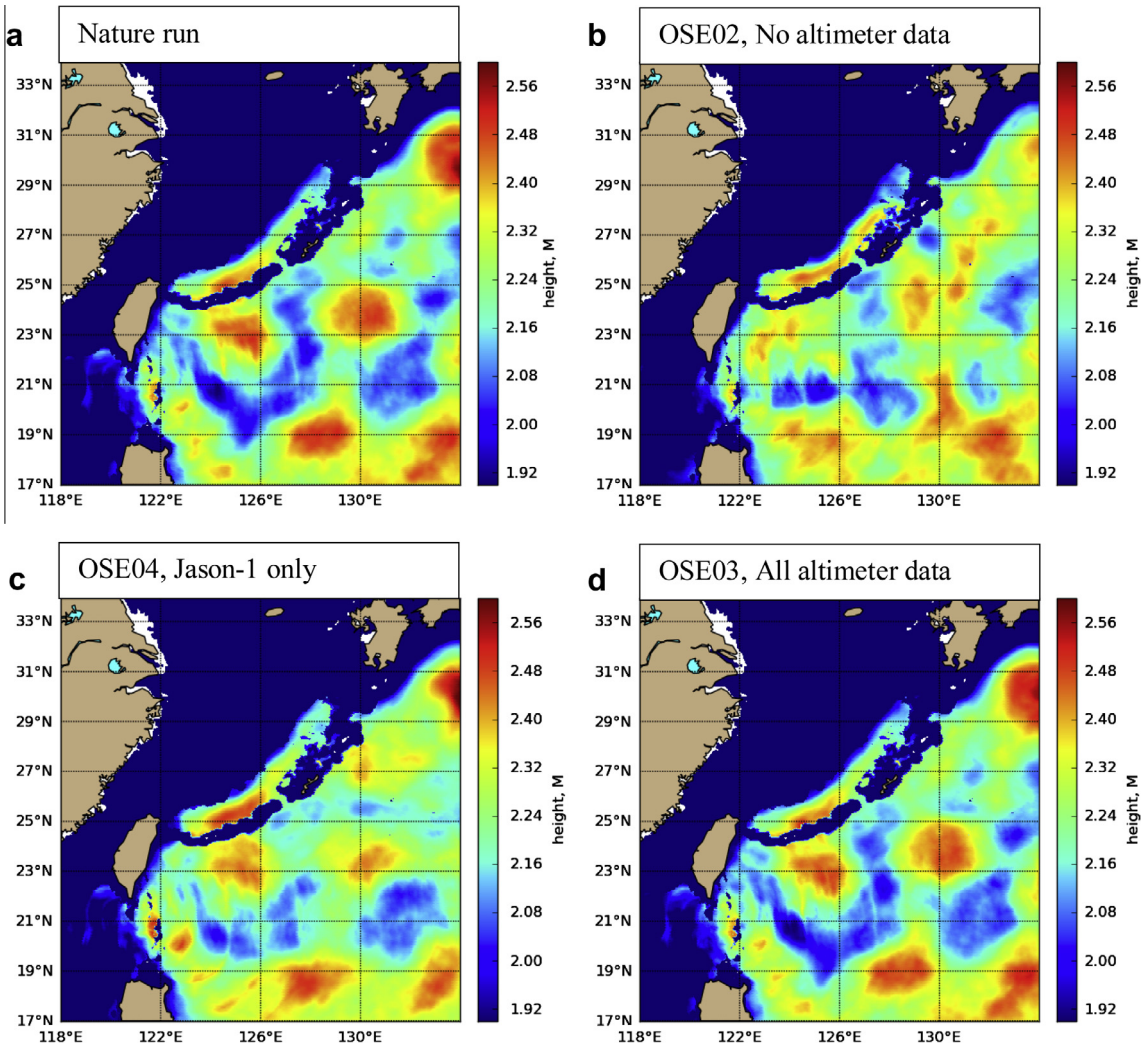

Fig. 8. The steric height from several of the OSEs provides initial confirmation that mesoscale field prediction has greater accuracy with increased data. The steric height from the nature run (a) is quite different from the experiment with only *in situ* and satellite SST assimilated (b). With only one satellite altimeter (Jason-1) the rough position of mesoscale features is reproduced (c), and with all altimeter satellites (d) the mesoscale field is well reproduced.

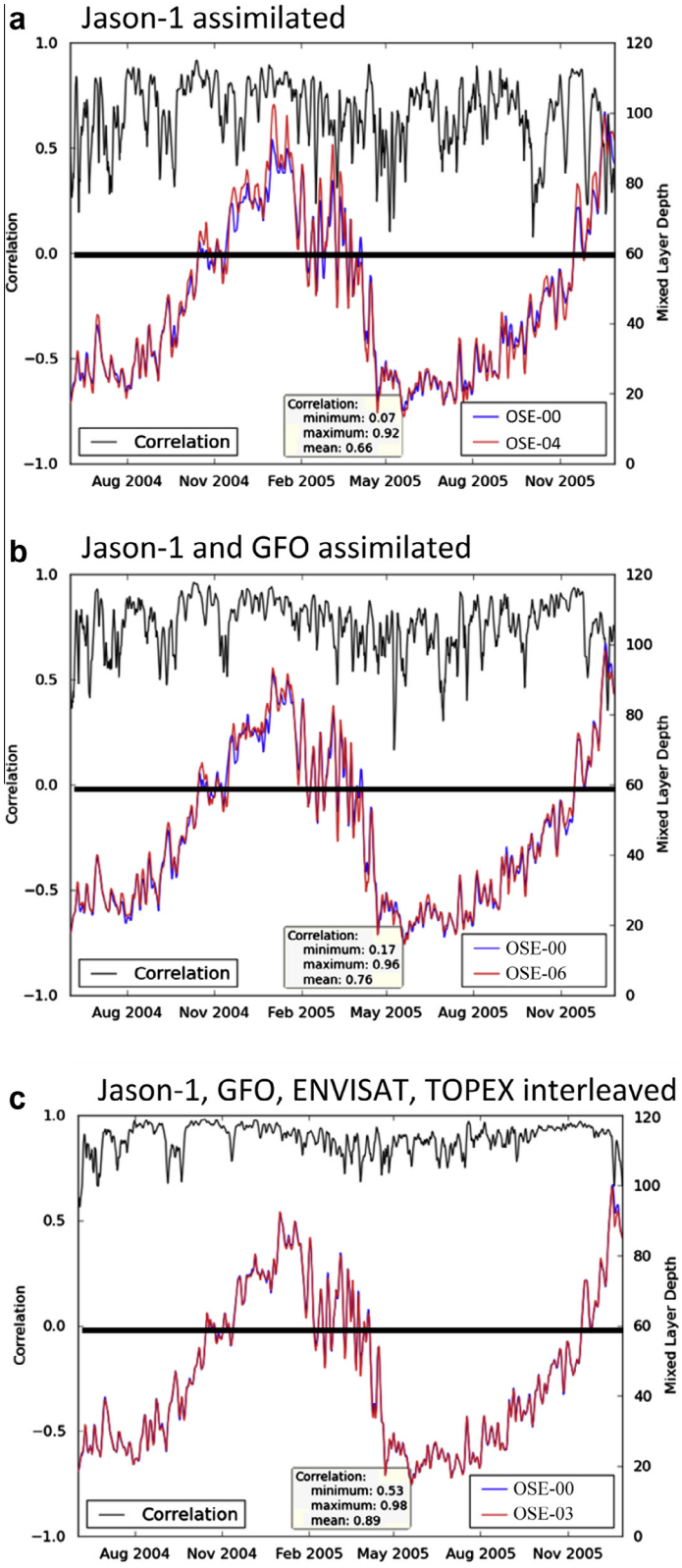

Fig. 9. MLD from the nature run is compared to MLD from several OSEs for the subdomain (20–24° N and 123–127° E) used in Fig. 6. The blue line is nature run MLD averaged over the subdomain and red line is the OSE MLD averaged over the subdomain. The seasonal cycle of MLD is apparent in all OSEs. The black line is the MLD correlation coefficient between the nature run and OSE over the subdomain. The minimum, maximum and time-averaged correlation coefficient are listed at the bottom of each plot. With one altimeter (a) the correlation is significant though frequently drops below the significance level of 0.62. The rate at which the correlation is below the significance level decreases with 2 satellite altimeter (b). Assimilating all 4 available altimeters results in the correlation always above the significance level (c).

plotted as the black lines in Fig. 9 with the minimum, maximum and time-averaged correlation values provided on plots. At times, the spatial correlation is quite small with only 1 or 2 altimeters assimilated. Increasing the number of altimeters assimilated increases the minimum, maximum and mean correlation. These analyses are repeated for the steric height, frontogenesis Q_1,

surface divergence and MLD for all OSEs, and the correlation for each OSE is listed in Table 1. Statistics in Table 1 are 3-hourly values averaged over the 1.5 years. For each time, the spatial mean is subtracted and spatial correlation computed. For Q_1, the correlation value is computed using the magnitude averaged over the upper 100 m.

A statistical t test to determine significance of the correlation, r, with n independent samples is given by:

$$t = r\sqrt{\frac{n-2}{1-r^2}} \tag{3}$$

Note that the different variables, steric height, Q_1, surface divergence and MLD, have different length scales and thus a different number of independent samples n. The estimated length scale for steric height and MLD is 100 km, while Q_1 and surface divergence have length scales of roughly 50 km. Under these conditions, a

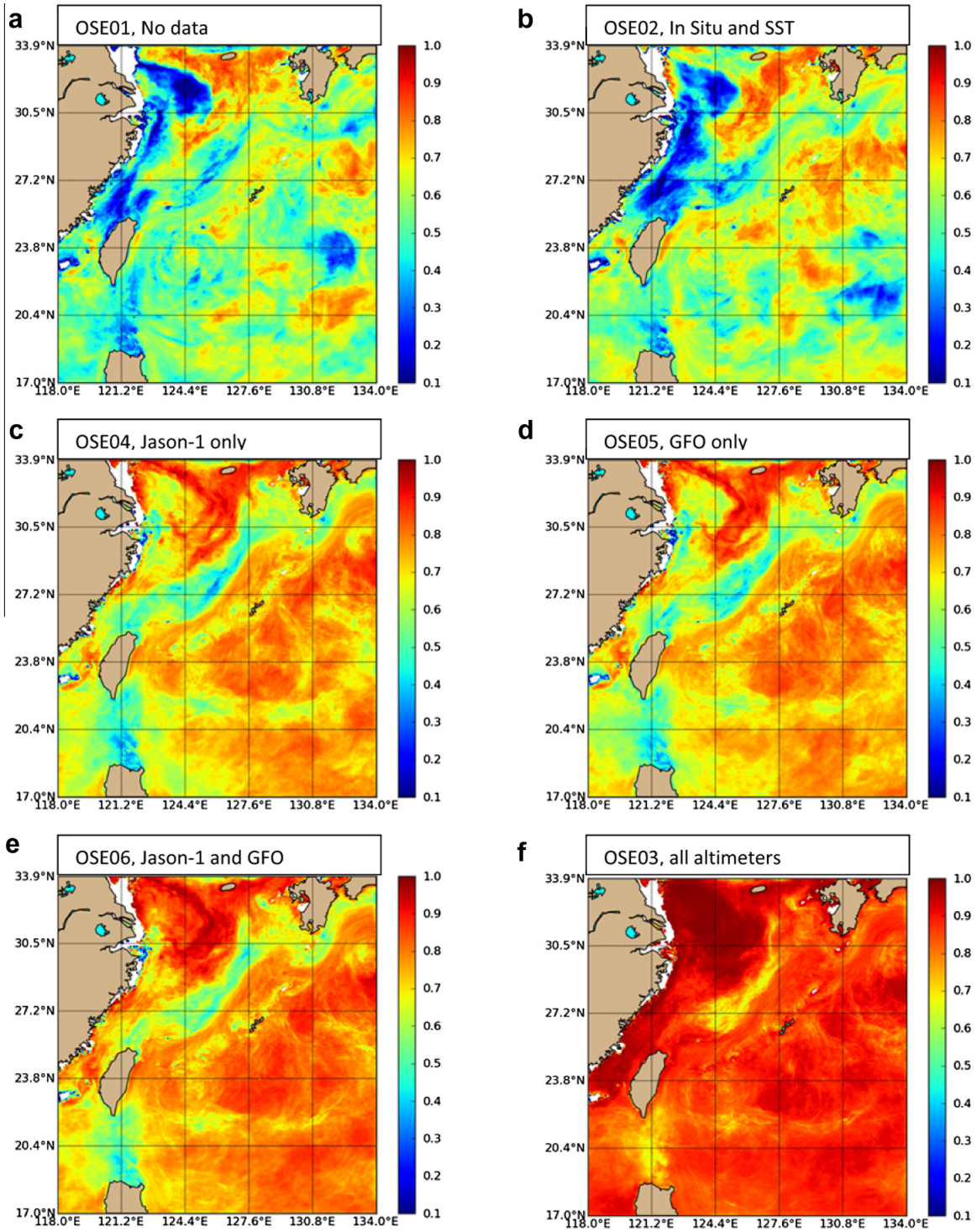

Fig. 10. The temporal correlation of MLD from the nature run and the OSEs constructed at each grid point using time series from which a 2 month boxcar filter has been applied and subtracted to remove long period variations. The results indicate increased skill as the number of altimeters increases as well as some spatial structure due to local processes affecting the skill. The correlations for OSEs with no data assimilate(a), all *in situ* data except altimeter (b), all *in situ* data with only Jason-1 altimetry (c), all *in situ* data with only GFO altimetry (d), all *in situ* data with only Jason-1 and GFO altimetry (e) and all *in situ* data with all altimeters (f) are shown.

one-sided 99% confidence t value must be greater than 2.96 or a correlation r greater than 0.62 at 100 km scales. For 50 km scales, confidence t value must be greater than 2.66 or a correlation r greater than 0.32. From Table 1, a statistically significant correlation of steric height or MLD occurs with 1 altimeter. A statistically significant correlation in Q_1 or surface divergence requires 2 altimeters.

The spatial structure of the temporal variability in predictive skill can be estimated for the MLD at each model grid point (Fig. 10). To consider subseasonal time scales, the correlation is estimated from MLD anomalies after high pass filtering using a two month boxcar filter. Increasing the number of altimeter data streams assimilated increases the skill consistent with temporal structure shown in Fig. 9. OSEs withholding all altimeters from the assimilation show no skill except in small patches as would be expected from coincidental correlation. The areas of maximal correlation are the area south of the Kuroshio and west of Japan on the continental shelf in all cases. Areas of minimal correlation are the north wall of the Kuroshio and the Luzon Strait. The north wall of the Kuroshio is dominated by small scale mesoscale eddies, and the Luzon Strait is an active area of Kuroshio intrusion into the South China Sea (Metzger and Hurlburt, 2001).

Correlation in the unobserved variables increases as data streams are added suggesting the unobserved variables are physically connected to the observed variables. The observed variable is SSH, through which the buoyancy field is inferred through historical covariances. The resulting currents drive the unobserved frontogenesis forcing Q_1 and subsequent unobserved divergence. Because of the strong relation between steric height and MLD (Fig. 7), a portion of MLD increased correlation is due to increased accuracy in positioning the mesoscale field. A second portion is attributed to increased accuracy in the positioning of the secondary circulation associated with the frontogenesis. The impact of these two different factors can be seen in comparing the trends of correlation as data streams are included within the steric height, Q_1, divergence and MLD.

Small-scale features associated with frontogenesis control MLD as well as the mesoscale features. If this is correct, MLD correlation should lie between that of the steric height due to ocean eddies and those of Q_1 and divergence driven by frontogenesis. The correlation statistics from all the OSEs are summarized in Fig. 11 as a function of the number of altimeters assimilated. Due to the multiple permutations of four satellites, several data points occur in the cases of 1, 2 and 3 altimeters. The marginal impact of adding satellites for the different variables is apparent. Steric height from 1 to 4 satellites rapidly increases asymptotically to near 1. Divergence and Q_1 increase roughly linearly from 1 to 4 satellites. Accurate prediction of Q_1 and divergence is very difficult with both reaching peak values just less than 0.6. MLD falls between steric height and Q_1 and divergence. The trend in MLD correlation is linear and higher than either Q_1 or divergence, reflecting the influence of both increased accuracy in positioning the eddy field at the larger scale and positioning the frontogenesis forcing as shown in Fig. 6 at the smaller scale.

6. Implications for observing systems

To enable skillful forecasting, observations are continually required to adjust a non-deterministic system state. Design of observing systems for such purposes is important. Prior studies to optimize sampling patterns for satellite altimeters have been conducted to understand how the orbit selection impacts analysis and forecast of the mesoscale (Holland and Malanotte-Rizzoli, 1989; Pujol et al., 2010). If the observation system does not provide sufficient resolution, the forecast error becomes very large (Oke et al., 2009). As numerical model resolution increases, models generate processes that are not resolved by present observing systems. The difference between model resolution and observing system resolution motivates consideration of the design and implementation of new observing platforms and sensor systems. A multiscale approach is desired where different observing systems can be applied to detect features at different scales (Lermusiaux, 2001).

Satellite altimeters do not directly observe nor correct frontogenesis forcing, upwelling, surface divergence and possible impact on MLD. The filament features are far from resolved or detected by the altimeter sea surface height observations, which are spaced about 6.5 km along the satellite track with distance between tracks of 300 km for TOPEX and Jason. Because the temperature variations due to the filaments affect only the upper portion of the ocean, steric height changes are below observation noise levels.

In general, *in situ* observations are not sufficient to resolve the frontogenesis spatial structure. Even with targeted high-resolution observations, the assimilation process within ocean prediction systems contains specifications for the decorrelation length scales that are roughly the Rossby radius of deformation. These length scales smooth out the 10–20 km filament signal that may occur in any observations, and the corrections obtained with the data assimilation scheme and covariances assume geostrophic balance. Thus, data assimilation, by itself, would tend to remove the filament features within the observations.

It follows that development of the frontogenesis filaments is entirely dependent on the dynamics of the model. The fact that the frontogenesis process is deterministically driven by the mesoscale field implies that the most important factor is accurate forecasting of the ocean eddies and fronts and the associated density and velocity fields. To this end, present observation systems and methods for assimilation are appropriate. The results here support continued maintenance of the present observation systems. As the density of observations is changed within the OSEs, the forecast skill for steric height as well as unobserved frontogenesis, surface divergence, and MLD change accordingly. Additional local observations would further refine prediction accuracy.

The required observing system can then be defined based on required skill from Figs. 9 or 11. This skill can be quantified either as a time-averaged correlation or as frequency with which the forecast skill drops below a threshold. Given the tolerance for either average skill or forecast failure rates, the observation system can be designed.

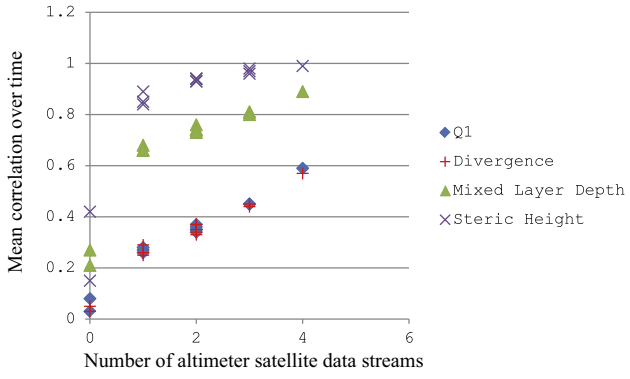

Fig. 11. The correlation coefficients from Table 1 are plotted as a function of number of satellite altimeters assimilated. The steric height correlation increases rapidly with just one data stream, and the marginal improvement of additional altimeters is small and decreases with increasing altimeters. The MLD marginal improvement is relatively constant from 1 to 4 altimeters. Frontogenesis Q_1 and surface divergence (vertical velocity) show a nearly linear increase in correlation as the number of altimeters assimilated increases and thus show a constant marginal improvement.

7. Conclusions

Frontogenesis as theorized by Hoskins (1982) is reproduced in numerical models. The mechanism in the simulations generating the upwelling and downwelling along the fronts is in agreement with prior model and theoretical studies demonstrating the forcing driven by horizontal buoyancy gradients increasing as the flow strains fluid parcels. Vertical velocities associated with filament frontogenesis are related to Q_1 and can be diagnosed by the omega Eq. (2). Thus there is consistency between the underlying mechanism related to the mesoscale ocean currents and buoyancy field. Correlation between the frontogenesis forcing and shallowing MLD is significant, particularly during fall through spring when MLD is conducive to being affected by the frontogenesis.

OSE experiments are performed in which satellite altimeter and *in situ* data sets are incrementally added for data assimilation. The increasing skill in forecasting the steric height indicates the improvement in predictability of the mesoscale field as additional observational datasets are assimilated (Fig. 10). In addition to the steric height, variables associated with the frontogenesis including Q_1 and surface divergence also show increased predictability as more satellite altimeter data are assimilated. Secondary effects relating small scale variations in MLD indicate predictive improvement as well. Caution should be exercised as the results here are based on assimilation experiments with real observations. The experiments cover a limited scope of dynamics that do not include processes such as mixed layer instabilities. These could alter the frontogenesis predictability.

Satellite SSH observations do not reliably detect the filament features within any of the associated variables. Therefore the systems examined here do not assimilate observations of the filaments. The only way the systems can reproduce the filaments is if the filaments are deterministically related to features that are observed. Following the theory of frontogenesis of Hoskins (1982), the filaments are forced by the mesoscale velocity and buoyancy fields and, thus, can be diagnosed from an accurate forecast of the mesoscale. From the OSE simulations, the conclusion emerges that frontogenesis filaments are predictable if the mesoscale field is accurately predicted. This result leads to the conclusion that the filaments have conditional deterministic predictability and are conditioned on an accurate prediction of the mesoscale.

This study that considers a simulated environment is one step toward the necessary demonstration in the real environment, which must be conducted. The skill in predicting frontogenesis in the OSEs not only improves confidence in the fidelity of existing forecast system, but also leads the application of ocean forecast systems into a realm not previously considered feasible, the operational prediction of ocean frontogenesis.

Acknowledgments

This research is supported in part by the project "Ageostrophic vorticity dynamics" sponsored by the Office of Naval Research (ONR) under program element 601153N and the CARTHE projects sponsored by the Gulf of Mexico Research Initiative. This paper is contribution NRL/JA/7320-11-1001 and has been approved for public release.

References

Ananda, P., Yannice, F., Gilles, L., Le Traon, P.-Y., 2006. Improved description of the ocean mesoscale variability by combining four satellite altimeters. Geophys. Res. Lett. 33, 13–16.

Barron, C.N., Kara, A.B., Martin, P.J., Rhodes, R.C., 2006. Formulation, implementation and examination of the vertical coordinate choices in the Global Navy Coastal Ocean Model (NCOM). Ocean Model. 11, 347–375.

Barron, C.N., Kara, A.B., Rhodes, R.C., Rowley, C., Smedstad, L.F., 2007. Validation Test Report for the 1/8 Global Navy Coastal Ocean Model Nowcast/Forecast System, NRL Tech Report NRL/MR/7320–07-9019. Naval Research Laboratory, Washington, DC.

Bell, M.J., Lefèbvre, M., Le Traon, P.-Y., Smith, N., Wilmer-Becker, K., 2009. GODAE: the global ocean data assimilation experiment. Oceanography 22 (3), 14–21. http://dx.doi.org/10.5670/oceanog.2009.62.

Boccaletti, G., Ferrari, R., Fox-Kemper, B., 2007. Mixed layer instabilities and restratification. J. Phys. Oceanogr. 37, 2228–2250. http://dx.doi.org/10.1175/JPO3101.1.

Capet, X., McWilliam, J.C., Molemaker, M.J., Shchepetkin, A.F., 2008a. Mesoscale to submesoscale transition in the California current system, part I: flow structure, eddy flux and observational tests. J. Phys. Oceanogr. 38, 29–43. http://dx.doi.org/10.1175/2007JPO3671.1.

Capet, X., McWilliam, J.C., Molemaker, M.J., Shchepetkin, A.F., 2008b. Meososcale to submesoscale transition in the California current system, part II: frontal processes. J. Phys. Oceanogr. 33, 44–64. http://dx.doi.org/10.1175/2007JPO3672.1.

Cummings, J.A., 2005. Operational multivariate ocean data assimilation. Q. J. R. Meteorolog. Soc. 131, 3583–3604.

Cummings, J., Bertino, L., Brasseur, P., Fukumori, I., Kamachi, M., Martin, M.J., Mogensen, K., Oke, P., Testut, C.E., Verron, J., Weaver, A., 2009. Ocean data assimilation systems for GODAE. Oceanography 22 (3), 96–109. http://dx.doi.org/10.5670/oceanog.2009.69.

Egbert, G.D., Erofeeva, S.Y., 2002. Efficient inverse modeling of barotropic ocean tides. J. Atmos. Oceanic Technol. 19, 183–204.

Fox, D.N., Barron, C.N., Carnes, M.R., Booda, M., Peggion, G., Gurley, J.V., 2002. The modular ocean data assimilation system. Oceanography 15, 22–28.

Garrett, G.J.R., Loder, J.W., 1981. Circulation and fronts in continental shelf seas. Philos. Trans. R. Soc. London, Ser. A 302, 563–581.

Goerss, J.S., 2009. Impact of satellite observations on the tropical cyclone track forecasts of the navy operational global atmospheric prediction system. Mon. Weather Rev. 137. http://dx.doi.org/10.1175/2008MWR2601.1.

Hodur, R.M., 1997. The naval research laboratory's couple ocean/atmosphere mesoscale prediction system. Mon. Weather Rev. 135, 1414–1430.

Holland, W.R., Malanotte-Rizzoli, P., 1989. Assimilation of altimeter data into an ocean circulation model: space versus time resolution studies. J. Phys. Oceanogr. 19, 1507–1534.

Hoskins, B.J., 1982. The mathematical theory of frontogenesis. Annu. Rev. Fluid Mech. 14, 131–151.

Hoskins, B.J., Bretherton, F.P., 1972. Atmospheric frontogenesis models: mathematical formulation and solution. J. Atmos. Sci. 29, 11–37.

Jacobs, G.A., Barron, C.N., Rhodes, R.C., 2001. Mesoscale characteristics. J. Geophys. Res. 106, 19581–19595.

Lermusiaux, P.F.J., 2001. Evolving the subspace of three-dimensional multiscale ocean variability: Massachusetts Bay. J. Mar. Syst. 29, 285–422.

Mahadevan, A., Tandon, A., 2006. An analysis of mechanisms for submesoscale vertical motion at ocean fronts. Ocean Model. 14, 241–256.

May, D.A., Parmeter, M.M., Olszewski, D.S., McKenzie, B.D., 1998. Operational processing of satellite sea surface temperature retrievals at the Naval Oceanographic Office. Bull. Am. Meteorol. Soc. 79, 397–407.

McWilliams, J.C., Molemaker, M.J., Olafsdottir, E.I., 2009a. Linear fluctuation growth during frontogenesis. J. Phys. Oceanogr. 39, 3111–3129.

McWilliams, J.C., Colas, F., Molemaker, M.J., 2009b. Cold filamentary intensification and oceanic surface convergence lines. Geophys. Res. Lett. 36, L18602. http://dx.doi.org/10.1029/2009GL039402.

Mensa, J.A., Garraffo, Z., Griffa, A., Ozgokmen, T., Haza, A., Veneziani, M., 2013. Seasonality of the submesoscale dynamics in the Gulf Stream region. Ocean Dyn.. http://dx.doi.org/10.1007/s10236-013-0633-1.

Metzger, E.J., Hurlburt, H.E., 2001. The nondeterministic nature of Kuroshio penetration and eddy shedding in the South China Sea. J. Phys. Oceanogr. 31, 2001.

Niewiadomska, K., Claustre, H., Prieur, L., d'Ortenzio, F., 2008. Submesoscale physical–biogeochemical coupling across the Ligurian Current (northwestern Mediterranean) using a bio-optical glider. Limnol. Oceanogr. 53, 2210–2225.

Oke, P.R., Balmaseda, M.A., Benkiran, M., Cummings, J.A., Dombrowsky, E., Fujii, Y., Guinehut, S., Larnicol, G., Le Traon, P.-Y., Martin, M.J., 2009. Observing system evaluations using GODAE systems. Oceanography 22 (3), 144–153. http://dx.doi.org/10.5670/oceanog.2009.72.

Paci, A., Caniaux, G., Gavart, M., Giordani, H., Lévy, M., Prieur, L., Reverdin, G., 2005. A high-resolution simulation of the ocean during the POMME experiment: simulation results and comparison with observations. J. Geophys. Res. 110 (C07S09). http://dx.doi.org/10.1029/2004JC002712.

Pallàs-Sanz, E., Johnston, T.M.S., Rudnick, D.L., 2010. Frontal dynamics in a California current system shallow front: 1. Frontal processes and tracer structure. J. Geophys. Res. 115, C12067. http://dx.doi.org/10.1029/2009JC006032.

Pinot, J.-M., Tintore, J., Wang, D.-P., 1996. A study of the omega equation for diagnosing vertical motions at ocean fronts. J. Mar. Res. 54, 239–259.

Pollard, R.T., Regier, L.A., 1992. Vorticity and vertical velocity at an ocean front. J. Phys. Oceanogr. 22, 609–625.

Pujol, M., Dobricic, S., Pinardi, N., 2010. Impact of multialtimeter sea level assimilation in the mediterranean forecasting model. J. Atmos. Oceanic Technol. 27, 2065. http://dx.doi.org/10.1175/2010JTECHO715.1.

Rosmond, T.E., Teixeira, J., Peng, M., Hogan, T.F., Pauley, R., 2002. Navy Operational Global Atmospheric Prediction System (NOGAPS): Forcing for ocean models. Oceanography 15, 99–108.

Smedstad, O.M., Hurlburt, H.E., Metzger, E.J., Rhodes, R.C., Shriver, J.F., Wallcraft, A.J., Kara, A.B., 2003. An operational eddy resolving 1/16° global ocean nowcast/forecast system. J. Mar. Syst. 40–41, 341–361.

Spall, M.A., 1995. Frontogenesis, subduction, and cross-front exchange at upper ocean fronts. J. Geophys. Res. 100, 2543–2557.

Thomas, L.N., Tandon, A., Mahadevan, A., 2008. Submesoscale processes and dynamics, ocean modeling in an eddying regime. In: Geophysical Monograph Series, vol. 177. American Geophysical Union, Washington, DC. http://dx.doi.org/10.1029/177GM04.

Zhong, Y., Bracco, A., 2013. Submesoscale impacts on horizontal and vertical transport in the Gulf of Mexico. J. Geophys. Res. 118, 1–18. http://dx.doi.org/10.1002/jgrc.20402.